Elasto-Plastic Finite Element Modeling of Short Carbon Fiber Reinforced 3D Printed Acrylonitrile Butadiene Styrene Composites

SUNIL BHANDARI [1,2,4] ROBERTO A. LOPEZ-ANIDO,[1,2,5]
LU WANG,[1,3,6] and DOUGLAS J. GARDNER[1,3,7]

1.—Advanced Structures and Composites Center, University of Maine, 35 Flagstaff Road, Orono, ME 04469, USA. 2.—Department of Civil and Environmental Engineering, University of Maine, 5711 Boardman Hall, Orono, ME 04469, USA. 3.—School of Forest Resources, University of Maine, 5755 Nutting Hall, Orono, ME 04469, USA. 4.—e-mail: sunil.bhandari@maine.edu. 5.—e-mail: rla@maine.edu. 6.—e-mail: lu.wang@maine.edu. 7.—e-mail: douglasg@maine.edu

This research extends the existing classical lamination theory based finite element (FE) models to predict elasto-plastic and bimodular behavior of 3D printed composites with orthotropic material properties. Short carbon fiber reinforced acrylonitrile butadiene styrene was selected as the 3D printing material. Material characterization of a 3D printed unidirectional laminate was carried out using mechanical tests. A bimodular material model was implemented using explicit FE analysis to predict the tension and bending behavior of a 3D printed laminate. The results of the FE model predictions were experimentally validated. Hill's yield function was effective at predicting the elasto-plastic stress–strain behavior of the laminate in tension. In bending, bimodular material behavior along with Hill's yield function worked reasonably well in predicting the elasto-plastic bending of the laminate. The material model proposed can be used to predict the mechanical behavior of 3D printed parts with complex geometry under complex loading and boundary conditions.

INTRODUCTION

The extrusion-based 3D printing process, also called fused deposition modeling (FDM) and fused filament fabrication (FFF), is currently the most common 3D printing process used for additive manufacturing of polymer composite parts.[1] An extrusion-based 3D printed part is produced by depositing beads of molten thermoplastic layer by layer which results in a part with orthotropic material properties.

Figure 1 shows the three principal material directions along with the three principal machine axes. Axes 1, 2 and 3 are the three principal material axes. Axes X, Y, and Z are the three principal machine axes and define the machine coordinate system described by ASTM/ISO 52900-15.[2] Material axis 1 is aligned with the direction of deposition of the bead. Material axis 2 lies in the same plane of deposition as material axis 1 and is perpendicular to material axis 1. Material axis 3 is normal to the plane of deposition. Angle θ is the angle between the global machine axis X and the material axis 1. E1, E2, and E3 are the Young's moduli along the principal material axes. Similarly, S1, S2, and S3 are the strengths along the 1, 2, and 3 axes respectively.

Researchers have used laminate analysis to model the mechanical behavior of 3D printed parts. Recent research works show that the linear elastic behavior of 3D printed parts under tension loading can be successfully modeled using CLT. Kulkarni and Dutta[3] developed an analytical model using laminate analysis to determine the elastic moduli of 3D printed laminates with layers oriented at different angles. Rodriguez et al.[4] introduced a strategy for optimizing the design of fused deposition modeling (FDM)-based 3D printed materials using laminate analysis. Li et al.[5] analyzed FDM-based 3D printed materials using laminate analysis and
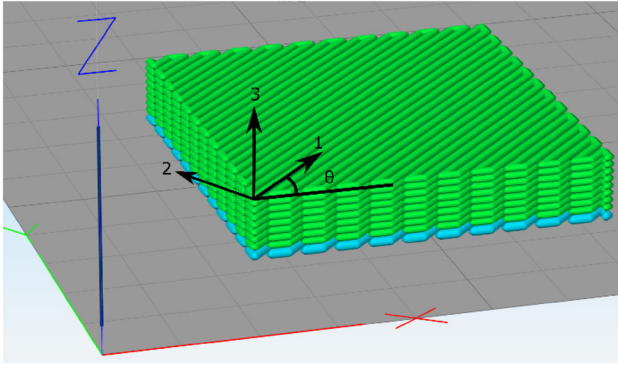
Fig. 1. Principal material axes and global axes for an extrusion-based 3D printed part.

proposed a set of equations to determine the elastic constants of FDM prototypes based on the analysis. Alaimo et al.[6] modeled the elastic behavior of FDM-based 3D printed material using classical lamination theory and used the Tsai-Hill yielding criterion to predict yielding of the 3D printed material in tension loading.

The difference in elastic response of some materials in compression compared to tension has been known for a long time[7,8]. Jones[9] discussed fiber reinforced polymers that have a tension modulus up to 40% higher than the compression modulus. Phan-Thein[10] discussed the bimodular behavior of short-fiber reinforced polymers and its implications regarding the use of high fiber aspect ratios for bending applications. Similar bimodular behavior has been observed in extrusion-based 3D printed parts. Ziemen et al.[11] reported a tensile modulus of 987 MPa and a compression modulus of 402 MPa for 3D printed acrylonitrile butadiene styrene (ABS) parts at $0°$ orientation. At $90°$ orientation, the tensile modulus was found to be 738 MPa and the compression modulus was found to be 382 MPa.[11] Song et al.[12] reported similar bimodular behavior in 3D printed PLA parts. An elastic modulus derived from bending tests would be useful in approximating the linear-elastic bending behavior of such bimodular materials at small deflections. However, when geometry, boundary conditions, and loadings are complex or yielding of materials is taken into account, the results from models based on bending elastic modulus deviate significantly from the experimental results.[10]

Different numerical techniques have been proposed to address the bimodular behavior of materials. Sun et al. reviewed different approaches to model the mechanical behavior of bimodular materials.[13] The two basic approaches generally used to model bimodular behavior are (1) Bert's model,[14] and (2) Ambartsumyan's model.[15] Bert's model uses either the tensile or compressive modulus based on whether the strains in the fiber are positive or negative. Ambartsumyan's model uses tensile or compressive modulus based on whether principal stress is positive or negative. Although not specific to 3D printed materials, Babesko et al.[16] proposed a numerical technique for analysis of the elasto-plastic stress–strain state of transversely isotropic shells with different moduli in compression and tension. Zhang et al.[17] discussed different numerical techniques to create a stabilized complementarity formulation for 3D bimodular materials. Li et al.[18] discussed different analytical solutions for functionally graded beams. A suitable material model should accurately predict the bending behavior of the 3D printed laminate.

In addition to the linear elastic bimodular behavior, the elasto-plastic behavior of the 3D printed parts also should be determined to accurately model the response of 3D printed material to different loadings. Hill's yield criterion and Tsai-Hill yield criterion have been used to model the yielding behavior of 3D printed materials.[6,19] Destrade et al.[20] showed that a simple finite element model cannot accurately predict the bending behavior of a bimodular material like bimodular rubber.

Different mechanical finite element models have been created for polymer extrusion-based 3D printed materials. Bhandari and Lopez-Anido[21,22] used space frame-based finite element models to generate effective homogenized properties for 3D printed cellular structures. Guessasma et al.[23] used finite element modeling to explain damage mechanisms in 3D printed polymers subject to severe compression. The finite element model used by Nouri et al.[24] predicted the transverse symmetry 3D printed ABS parts. Guessasma et al.[25] used finite element modeling to point out the combination of local shearing and inhomogeneous stretching that correlated to the filament arrangement in 3D printed PETG (polyethylene terephthalate glycol) parts within the plane of construction. Werken et al.[26] discussed different considerations for developing a suitable finite element model for 3D printed parts. Xu et al.[27] used finite element modeling to predict the deformation of disordered lattice structures. Somireddy et al.[19,28,29] developed a constitutive material model and used classical lamination theory (CLT) and nonlinear finite element analysis with Hill's yield criteria and first ply failure to predict the bending response of 3D printed ABS parts. While these models are quite successful in predicting the tensile and compressive behavior of the 3D printed material, a CLT based finite element model that considers the bimodular linear elastic behavior and yielding would be useful in predicting yielding and bending responses of 3D printed short carbon fiber reinforced polymer parts.

Elasto-Plastic Finite Element Modeling of Short Carbon Fiber Reinforced 3D Printed Acrylonitrile Butadiene Styrene Composites

477

This research work aims to extend the existing CLT-based linear-elastic finite element analysis used for modeling the mechanical response of 3D printed composite parts by addressing the bimodular and elasto-plastic behavior of 3D printed composite materials.

Progressive damage and ultimate strength prediction are beyond the scope of this article. Past research work has shown that post ultimate strength behavior in short-fiber reinforced composite laminate needs to incorporate lamina strength parameters in different directions,[30] progressive fiber/matrix debonding in short-fiber reinforced composites,[31] and progressive fracture mechanisms.[32]

The objectives of this research work were: (1) implement a bimodular elasto-plastic material finite element model to describe the bending behavior of a 3D printed short carbon fiber reinforced ABS part, and (2) validate the bimodular elasto-plastic material finite element model experimentally.

MATERIALS AND METHODS

Modeling Approach for 3D Printed Material

The 3D printed parts were modeled as shells with stacked layers of orthotropic laminae oriented at different angles. The shell was homogenized using laminate analysis. The material behavior was divided into linear elastic and elasto-plastic regions.

Linear Elastic Behavior

Several material models have been discussed by researchers to efficiently implement the linear elastic bimodular behavior of the material in a finite element model.[33–36] This study uses a simple 2D orthotropic material model for a lamina based on Ambartsumyan's constitutive equations[15] for bimodular materials, where elastic constants are updated based on whether the element is under tension or compression. This simple implementation was chosen because it allows for easy incorporation of elasto-plastic behavior into the finite element model through Hill's yielding function. This process might result in element stiffness matrices that are not symmetric.

The user-defined material subroutine in Abaqus, VUMAT, was used to define the material behavior. Equation 1 shows the in-plane stress–strain relationship for the material.

$$\begin{Bmatrix} \varepsilon_1 \\ \varepsilon_2 \\ \gamma_6 \end{Bmatrix} = \begin{bmatrix} \frac{1}{E_1} & -\frac{v_{21}}{E_2} & 0 \\ -\frac{v_{12}}{E_1} & \frac{1}{E_2} & 0 \\ 0 & 0 & \frac{1}{G_{12}} \end{bmatrix} \begin{Bmatrix} \sigma_1 \\ \sigma_2 \\ \sigma_6 \end{Bmatrix}$$

$$\text{and } \varepsilon_3 = -\frac{v_{13}}{E_1}\sigma_1 - \frac{v_{23}}{E_2}\sigma_2 \tag{1}$$

where ε_1 = strain in the 1-direction of the material. ε_2 = strain in the 2-direction of the material. γ_6 = engineering shear strain in the 1–2 plane of the material. E_1 = Young's modulus in the 1-direction of the material. E_2 = Young's modulus in the 2-direction of the material. v_{21} = Poisson's ratio for loading in the 2-direction of the material. v_{12} = Poisson's ratio for loading in the 1-direction of the material. G_{12} = shear modulus in the 1–2 plane of the material.

Since the material shows a bimodular nature, with different modulus in compression and tension, the Young's moduli and the corresponding Poisson's ratios are defined based on whether the normal stresses along material axes are positive or negative. This scheme has been implemented using Eqs. 2 through 5.

$$E_1 = \left\langle \frac{\sigma_1}{|\sigma_1|} E_1^t \right\rangle + \left\langle \frac{-\sigma_1}{|\sigma_1|} E_1^c \right\rangle \tag{2}$$

$$E_2 = \left\langle \frac{\sigma_2}{|\sigma_2|} E_2^t \right\rangle + \left\langle \frac{-\sigma_2}{|\sigma_2|} E_2^c \right\rangle \tag{3}$$

$$v_{12} = \left\langle \frac{\sigma_2}{|\sigma_2|} v_{12}^t \right\rangle + \left\langle \frac{-\sigma_2}{|\sigma_2|} v_{12}^c \right\rangle \tag{4}$$

$$v_{21} = \left\langle \frac{\sigma_2}{|\sigma_2|} v_{21}^t \right\rangle + \left\langle \frac{-\sigma_2}{|\sigma_2|} v_{21}^c \right\rangle \tag{5}$$

where E_1^t = Young's modulus in the 1-direction in tension. E_1^c = Young's modulus in the 1-direction in compression. E_2^t = Young's modulus in the 2-direction in tension. E_2^c = Young's modulus in the 2-direction in compression. v_{12}^t = Poisson's ratio for loading in the 1-direction in tension. v_{12}^c = Poisson's ratio for loading in the 1-direction in compression. v_{21}^t = Poisson's ratio for loading in the 2-direction in tension. v_{21}^c = Poisson's ratio for loading in the 2-direction in compression. σ_1 = normal stress in the 1-direction. σ_2 = normal stress in the 2-direction. $||$ is an absolute value operator. $\langle \rangle$ is a Macaulay operator, defined as: $\langle a \rangle = a$ if a is positive. $\langle a \rangle = 0$ if a is negative.

Abaqus explicit solver is used to solve for the stresses in material with each time increment. Because the material exhibits bimodular behavior, a sudden change in matrix stiffness occurs when the stress direction is changed. The Jacobian matrix of the system is necessary for implicit solvers and the Jacobian matrix is not well defined in the region of sudden stiffness change. Various implicit models have been developed to overcome the limitation.[37,38] However, for this research work, an explicit solver is adequate as it can provide solutions in a reasonable amount of time.

The stress vector at the kth time step using indicial notation is

$$\sigma_i^k = \sigma_i^{k-1} + Q_{ij}^k d\varepsilon_j^k \tag{6}$$

where σ_i^{k-1} = stress vector at $(k-1)$th time step. Q_{ij}^k = laminate stiffness matrix at the kth time step. $d\varepsilon_j^k = \varepsilon e_j^k - \varepsilon e_j^{k-1}$ = elastic strain increment at the kth time step.

Yielding Behavior

Several suitable elasto-plastic models are discussed in the literature for composite materials.[39–41] A simple elasto-plastic model for orthotropic materials was adopted. The incremental formulation with isotropic work hardening was assumed. The components of the total strain increment at the kth time step are:

$$d\varepsilon_j^k = d\varepsilon e_j^k + d\varepsilon p_j^k \tag{7}$$

where $d\varepsilon e_j^k$ = elastic component of the total strain increment at the kth time step. $d\varepsilon p_j^k$ = plastic component of the total strain increment at the kth time step

The total stress increment at the kth time step caused by the elastic strain is

$$d\sigma_i^k = Q_{ij}^k d\varepsilon e_j^k \tag{8}$$

Where Q_{ij}^k = laminate stiffness matrix at the kth time step. $d\varepsilon e_j^k$ = elastic portion of the total strain increment at the kth time step.

The Hill's quadratic yield function adopted is

σ_1 = axial stress in the 1-direction. σ_2 = axial stress in the 2-direction. σ_6 = shear stress in the 1–2 plane.

The yield ratios are calculated based on whether the $\sigma 1$ for the element is positive or negative. The plastic hardening curve (stress vs plastic strain) is also used based on whether $\sigma 1$ is positive or negative. If $\sigma 1$ is positive, the plastic hardening curve from tension tests in 1-direction is used, else the plastic hardening curve from compression test in 1-direction is used. The equivalent plastic strain is

$$d\lambda^k = \frac{n_j^k Q_{ij}^k d\varepsilon_i^k}{n_j^k Q_{ij}^k n_i^k + h^k} \tag{11}$$

where $n_j^k = \frac{\partial f(\sigma)}{\partial \sigma_j^k}$. $d\varepsilon_i^k$ is the total strain increment at the kth time step. $h^k = \frac{d\sigma_i^k}{d\varepsilon p_j^k}$ is the strain hardening coefficient, the slope of the stress vs plastic strain curve at a given stress at the kth time step

The total stress increment from Eq. 8 is rewritten as a function of the strain increment and the plastic multiplier, as follows

$$d\sigma_i^k = Q_{ij}^k \left(d\varepsilon_j^k - d\lambda^k \cdot n_j^k\right) \tag{12}$$

The algorithm proposed by Dunne and Petrinic[41] is used to calculate the stress and strain increment at each update. The algorithm evaluates the yield function and determines if the material is actively

$$f(\sigma) = \sqrt{F(\sigma_{22} - \sigma_{33})^2 + G(\sigma_{33} - \sigma_{11})^2 + H(\sigma_{11} - \sigma_{22})^2 + L\sigma_{23}^2 + M\sigma_{31}^2 + N\sigma_{12}^2} \tag{9}$$

where $F = \frac{1}{2}\left(\frac{1}{R_{22}^2} + \frac{1}{R_{33}^2} - \frac{1}{R_{22}^2}\right)$. $G = \frac{1}{2}\left(\frac{1}{R_{33}^2} + \frac{1}{R_{11}^2} - \frac{1}{R_{22}^2}\right)$. $H = \frac{1}{2}\left(\frac{1}{R_{11}^2} + \frac{1}{R_{22}^2} - \frac{1}{R_{33}^2}\right)$. $L = \frac{3}{R_{23}^2}$. $M = \frac{3}{R_{31}^2}$. $N = \frac{3}{R_{12}^2}$. σ_1 = normal stress in the 1-direction. σ_2 = normal stress in the 2-direction. σ_3 = normal stress in the 3-direction. σ_{23} = shear stress in the 2–3 plane. σ_{31} = shear stress in the 3–1 plane. σ_{12} = shear stress in the 1–2 plane. $R_{11}, R_{22}, R_{33}, R_{23}, R_{31}, R_{12}$ are the orthotropic yield stress ratios

The Hill's yield function for plane stress conditions is reduced from Eq. 9, as follows:

$$f(\sigma) = \sqrt{F(\sigma_{22}^2) + G(\sigma_{11}^2) + H(\sigma_{11} - \sigma_{22})^2 + N\sigma_{12}^2} \tag{10}$$

where $R_1 = \frac{\sigma_{y1}^2}{\sigma_y^2} = 1.0$. $R_2 = \sigma_{y1}^2/\sigma_{y2}^2$. $R_6 = 3\sigma_{y1}^2/\sigma_{y6}^2$. σ_{y1} = yield stress determined from uniaxial tests in the 1-direction. σ_{y2} = yield stress determined from uniaxial tests in the 2-direction. σ_{y6} = yield stress determined from shear tests in the 1–2 plane.

yielding. If the material is actively yielding, it calculates the plastic multiplier, stress increment and isotropic hardening increment. The algorithm finally updates all the quantitates to the end of the time increment using explicit integration.

Experimental Methods

Experiments were carried out for material characterization to generate input material properties for the finite element model. Seven elastic constants $E_{1t}, E_{2t}, v_{12t}, G_{12}, E_{1c}, E_{2c}, v_{12c}$ along with five yield stresses $S_{1yt}, S_{2yt}, S_{1yc}, S_{2yc}, S_{12y}$, and two strain hardening curves for tension in the 1-direction and compression in the 1-direction were necessary for the finite element modeling the elasto-plastic behavior of the 3D-printed carbon-ABS parts.

Material Characterization Experiments

Material characterization tests were carried out to determine the material properties required for

finite element modeling. 3D printed unidirectional test specimens were used to determine the material properties. A Lulzbot Taz 6 printer was used for printing the specimens. CarbonX CFR-ABS filament from 3Dxtech was used. Laminates with nine layers were printed using the printing parameters listed in Table I.

Mechanical characterization of the 3D printed laminate in tension, compression, and shear was conducted according to ASTM D638, ASTM D6641, and ASTM D7078, respectively. All specimens were prepared on a water jet and conditioned at 50% relative humidity and a temperature of 23°C before evaluation. The strain was measured during each experiment using ARAMIS, a non-contact digital image correlation (DIC) system.[42,43]

All mechanical tests were carried out on a servo-hydraulic Instron testing frame. A 1-kN load cell was used for tension, compression and shear tests. A 200-N load cell was used for bending tests. The crosshead displacement rate for the tension tests was 5 mm/min per ASTM D638. The crosshead displacement rate for the compression tests was 1.3 mm/min. The crosshead displacement rate for the shear tests was 2 mm/min.

Validation Experiments

Two validation experiments were carried out to compare and verify the results from the finite element modeling. An ASTM D638 test was carried out on six specimens prepared from a laminate printed with [0°/−45°/45°/90°/0°/90°/45°/−45°/0°] orientation with each layer of thickness 0.36 mm. An ASTM D790 test was carried out on six specimens prepared from the laminate mentioned above.

Finite Element Model

Eight test cases were evaluated using linear, linear bimodular, and bimodular yielding material models. The test cases with different material behaviors considered are listed in Table II.

The material properties obtained from tension, compression and shear tests were used as input properties for the model. The weakness in the interlayer bonds is incorporated in the model by the Young's modulus (T2) in the 90° orientation laminates, the shear modulus (G23) across beads as shown in Table III. The interlayer weakness is also incorporated in the model via the Hill's yield constants that govern the yielding behavior of the material in the model.

An ASTM D638 tension test and an ASTM D790 bending test were simulated using finite element modeling. Abaqus 6.13 was used for finite element modeling. A user-defined material model was used to define the stress–strain behavior of the unidirectional material.

A 2D planar deformable shell part was created with dimensions corresponding to ASTM D638 type

Table I. Printing parameters for the 3D printed specimens

Parameter	Value
Nozzle diameter	0.8 mm
Retraction distance	1.5 mm
Retraction speed	90 mm/s
Layer height	0.36 mm
Outline perimeters/shells	0
Top/bottom solid layers	0
Infill	None
Extruder temperature	240°C
Bed temperature	110°C
Printing speed	60 mm/s
Printing speed for the first layer	12 mm/s
Movement speed	60 mm/s
Layer cooling fan	Off

Table II. Finite element models used for the study and the input properties

Material behavior	Test	Input properties
Linear Elastic with tension modulus	Tension	$E_{1t}, E_{2t}, v_{12t}, G_{12}$
Hill's yielding with tension modulus	Tension	$E_{1t}, E_{2t}, v_{12t}, G_{12}, S_{1yt}, S_{2yt}, S_{12y}$, strain hardening curve in T1 direction
Linear elastic with tension modulus	Bending	$E_{1t}, E_{2t}, v_{12t}, G_{12}$
Linear elastic with compression behavior	Bending	$E_{1c}, E_{2c}, v_{12c}, G_{12}$
Linear elastic with bimodular behavior	Bending	$E_{1t}, E_{2t}, v_{12t}, G_{12}$ E_{1c}, E_{2c}, v_{12c}
Elasto-plastic with tension modulus and Hill's yield criterion	Bending	$E_{1t}, E_{2t}, v_{12t}, G_{12}, S_{1yt}, S_{2yt}, S_{12y}$, strain hardening curve in T1 direction
Elasto-plastic with compression modulus and Hill's yield criterion	Bending	$E_{1c}, E_{2c}, v_{12c}, G_{12}, S_{1yc}, S_{2yc}, S_{12y}$, strain hardening curve in C1 direction
Elasto-plastic with bimodular behavior and Hill's yield criterion	Bending	$E_{1t}, E_{2t}, v_{12t}, G_{12}, S_{1yt}, S_{2yt}, S_{12y}$, strain hardening curve in T1 direction $E_{1c}, E_{2c}, v_{12c}, S_{1yc}, S_{2yc}, S_{12y}$, strain hardening curve in C1 direction

Table III. Mechanical properties from material characterization tests (COV values in parentheses)

	T1 (0°)	T2 (90°)	C1 (0°)	C2 (90°)	G13 (between beads)	G23 (across beads)
Modulus (GPa)	5.70 (1.5%)	2.17 (6.5%)	3.58 (6.7%)	2.32 (5.4%)	0.851 (3.9%)	0.909 (5.0%)
Ultimate Strength (MPa)	44.3 (0.43%)	13.74 (15%)	60.5 (1.6%)	49.3 (1.0%)	24.2 (5.7%)	25.1 (3.9%)
0.2% offset strength (MPa)	41.7 (0.56%)		57.4 (3.1%)	41.2 (8.6%)	20.0 (10%)	19.6 (15%)
Poisson's ratio	0.392 (6.6%)	0.161 (18.0%)	0.391 (7.0%)	0.137 (7.7%)	–	–
0.05% offset strength (MPa)	21.5 (0.25%)	12.9 (8.3%)	23.5 (4.4%)	21.4 (3.3%)	14.4 (7.5%)	14.0 (8.2%)
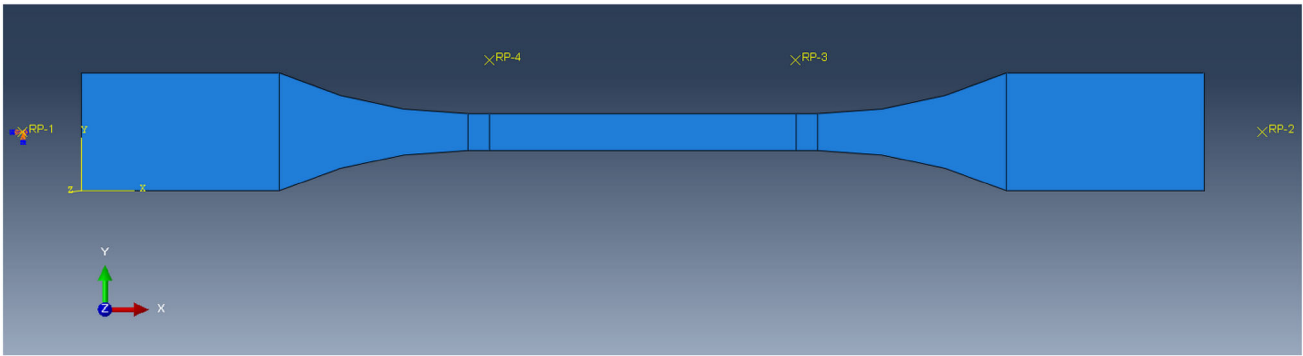
Fig. 2. Finite element model of ASTM D638 type II specimen for tension.

II specimen. Another 2D planar deformable shell part was created with dimensions corresponding to ASTM D790 bending specimen. A composite layup was defined with [0/−45/45/90/0/90/45/−45/0] orientation with each layer being 0.36 mm thick. Each layer was assigned three integration points. An explicit dynamic solving step was defined. The time increment was defined automatically by Abaqus.

For the tension test finite element models, constant displacement of 5 mm/minute was applied at one gripping end and another gripping end was kept fixed. Reference point 1 was used for measuring reaction force and for applying the fixed boundary condition. Reference point 2 was used to apply displacement to the gripping end of the specimen. Reference points 3 and 4 were used for measuring the displacement of the gauge section. The reference points and the boundary conditions for the model are shown in Fig. 2. An S4R element, which defines a 4-node doubly curved thin or thick shell, with reduced integration, and hourglass control for finite membrane strains was used for meshing. An S3R element, which is a 3-node triangular thin or thick shell, finite membrane strain element, was used if the curved geometry of the specimen did not allow for quadrilateral elements. A mesh with 2301 linear quadrilateral elements and 14 linear triangular elements was obtained. A total of 2513 nodes were created for the analysis. Mesh convergence for the tension test finite element model was verified by plotting the maximum reaction force vs the number of nodes in the model.

For the bending test finite element models, constant displacement of 5 mm/min applied at the center and simply a supported boundary condition was applied at the support positions. Reference point 1 was used for applying the displacement. The reference points and the boundary conditions for the model are shown in Fig. 3. An S4R element, which defines a 4-node doubly curved thin or thick shell, with reduced integration, and hourglass control for finite membrane strains was used for meshing. A mesh with 1378 linear quadrilaterals was obtained. A total of 1498 nodes were created for the analysis. Mesh convergence for the bending test finite element model was verified by plotting the maximum reaction force at reference point 1 versus the degrees of freedom in the model.

RESULTS AND DISCUSSIONS

Material Characterization Tests

The results from the material characterization experiments are listed in Table III.

It was observed that Young's modulus in tension in the 1-direction is 1.53 times the compression modulus. However, the Young's modulus in tension in the 2-direction is 0.93 times the compression modulus. For tension tests in the 2-direction, the material failure was comparatively brittle and 0.2%
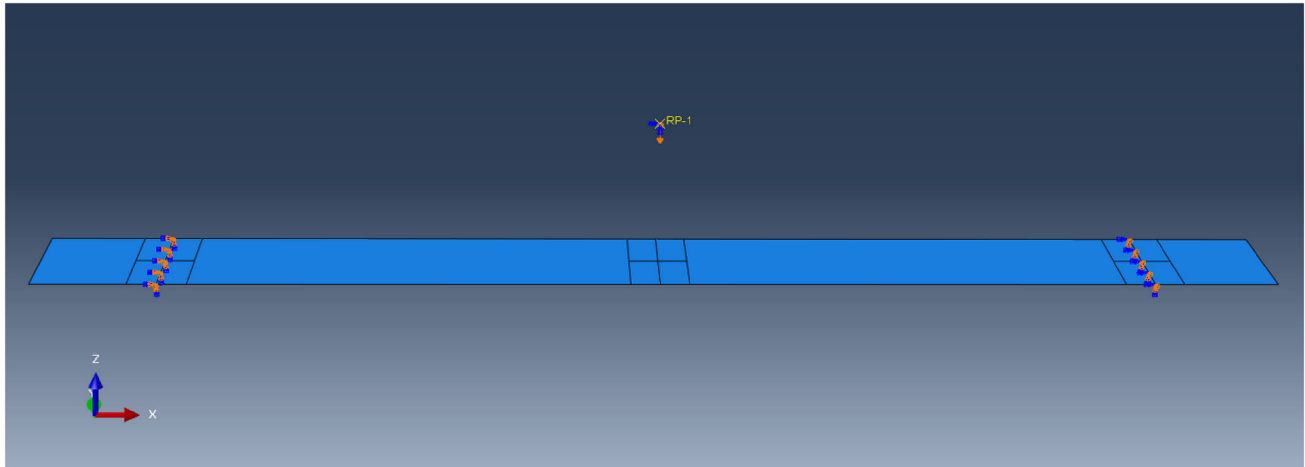
Elasto-Plastic Finite Element Modeling of Short Carbon Fiber Reinforced 3D Printed Acrylonitrile Butadiene Styrene Composites

481

Fig. 3. Finite element model of ASTM D790 specimen for bending.

Table IV. Summarized results from the finite element models

Material behavior	Test	Results
Linear elastic with tension modulus	Tension	Elastic modulus of the 3D printed laminate from the model (3.26 MPa) matched closely with the experimental results (3.46 MPa)
Hill's yielding with tension modulus	Tension	Elastic modulus and elasto-plastic yielding behavior matched closely with experimental results as shown in Fig. 4
Linear elastic with tension modulus	Bending	Over-predicted bending stiffness (6.94 N/mm) by 17%
Linear elastic with compression behavior	Bending	Under-predicted bending stiffness (4.90 N/mm) by 17%
Linear elastic with bimodular behavior	Bending	Bending stiffness from the model (5.80 N/mm) matched closely with the experimental results (5.90 N/mm)
Elasto-plastic with tension modulus and Hill's yield criterion	Bending	Over-predicted tangent bending stiffness, under-predicted ultimate load as shown in Fig. 7
Elasto-plastic with compression modulus and Hill's yield criterion	Bending	Under-predicted tangent bending stiffness, over-predicted ultimate load as shown in Fig. 7
Elasto-plastic with bimodular behavior and Hill's yield criterion	Bending	Slightly under-predicted tangent bending stiffness and ultimate load as shown in Fig. 7

offset strength could not be calculated. The bimodular behavior is more pronounced in the direction of fiber alignment, and the observation is consistent with the assumption made by Phan-Thein[10] that the cause of bimodularity is related to the short carbon fiber and not the matrix. Researchers[44] have explained that the difference in Young's modulus in compression and tension is caused by a difference in loading rate. However, in this research work, cross-head displacement for compression was 1.3 mm/min for a gage length of 13 mm while that for tension specimens was 5 mm/min for a gage length of 50 mm. The strain rates measured by the DIC system in the gage area were very close in compression and tension for the linear-elastic portion of the test.

Significant yielding occurs before the material reaches 0.2% offset strength. While the 0.2% offset strength serves well for predicting yielding failure with Hill's yield criteria, the initiation of yielding occurs much earlier. A 0.05% offset strength was assumed as the initiation point of yield. The Hill's yield constants were also calculated based on 0.05% offset strength.

Finite Element Model and Results

Table IV summarizes the results from the eight test cases used for the study.

Figure 4 shows the stress–strain behavior of the tension specimens. The finite element model with linear elastic behavior closely predicts the linear elastic behavior of the laminate under tension. The Young's modulus of the laminate as predicted by the finite element model is 3.27 GPa, whereas that predicted by laminate analysis is 3.26 GPa. The Young's modulus calculated from validation experiments is 3.46 GPa with a COV of 1.003%. Elasto-
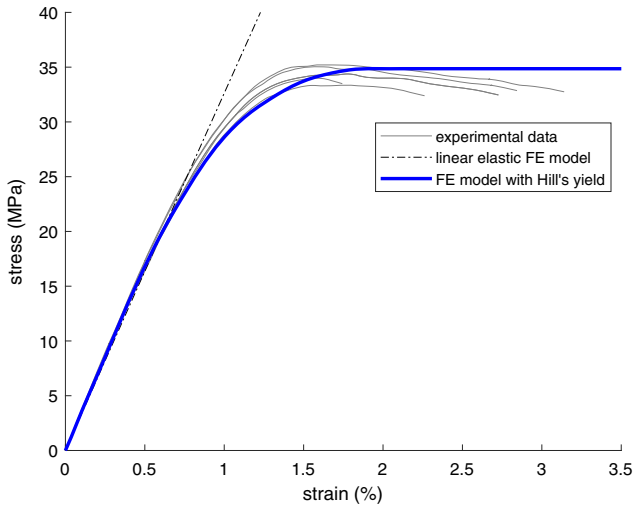
Fig. 4. Stress vs strain plot from experiments and the finite element models of the tension tests.
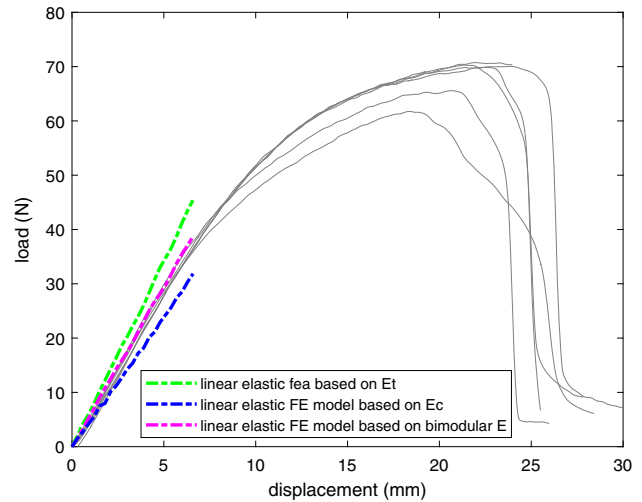

Fig. 6. Load-deflection plot from the bending experiments and the bending finite element model using compression behavior, tension behavior, and bimodular behavior.
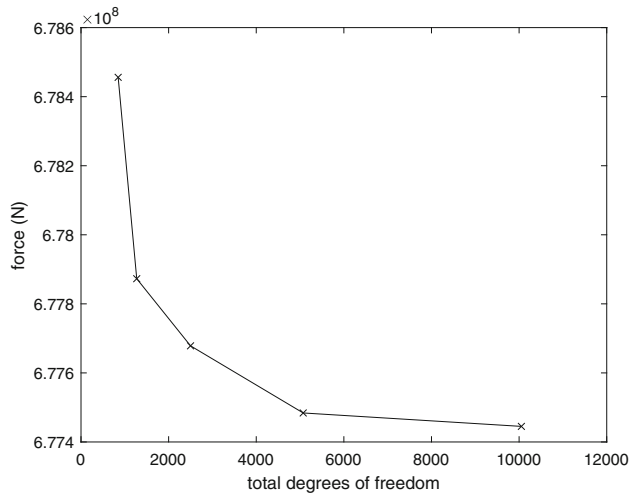

Fig. 5. Mesh convergence for the tension test finite element model considering yielding.

plastic tensile behavior of the test laminate predicted by the finite element model that used Hill's yielding function closely matched the experimental results. In the tension tests, all the layers experience equal tensile strain. The 0° layers reach the yield stress earlier because they have higher modulus along the loading direction.

The mesh convergence plot for the tension test finite element model is shown in Fig. 5.

Figure 6 shows the load vs deflection behavior of the bending specimens. In bending, the top and the bottom layers experience higher strains compared to the middle layers. It was observed that the bottom layer started yielding earlier than the top layer.

Because a specimen under a bending load experiences tension as well as compression forces, assigning the tensile Young's modulus for the entire

beam over-predicts the bending stiffness whereas assigning the compression Young's modulus for the entire beam under-predicts the bending stiffness of the beam. Considering the bilinear behavior with tension modulus for regions in tension and compression modulus for regions in compression results in a load–displacement curve that tracks the experimental data closely. The bending stiffness from the model considering the tension modulus is 6.94 N/mm and that from the laminate analysis is 6.88 N/mm. The bending stiffness from the finite element model considering the compression modulus is 4.90 N/mm and that from the laminate analysis is 4.73 N/mm. The bending stiffness from the finite element model that accounts for the bimodular nature of the material is 5.80 N/mm. The bending stiffness calculated from experimental data is 5.90 N/mm.

Figure 7 shows the results from the finite element analysis that accounts for Hill's yielding. Mean maximum load sustained by the beams in experimental bending tests was 69.1 N. The model that used the tension modulus, Hill's yield constants, and the plastic hardening curve derived from the tension tests over-predicted the bending stiffness by 17% in the linear-elastic range. However, the beam section withstood a maximum load of 52.8 N, which was 24% lower than the loads observed during the mechanical tests.

The model that used the compression modulus, and yield parameters derived from compression tests predicted the maximum load on the beam section at a higher load of 79.4 N, which was 15% higher than mean experimental maximum load. However, the stiffness predicted by the model was lower by 17% in the linear-elastic range compared to the experimental results. The displacement at the maximum load was higher by 12% compared to

Elasto-Plastic Finite Element Modeling of Short Carbon Fiber Reinforced 3D Printed Acrylonitrile Butadiene Styrene Composites
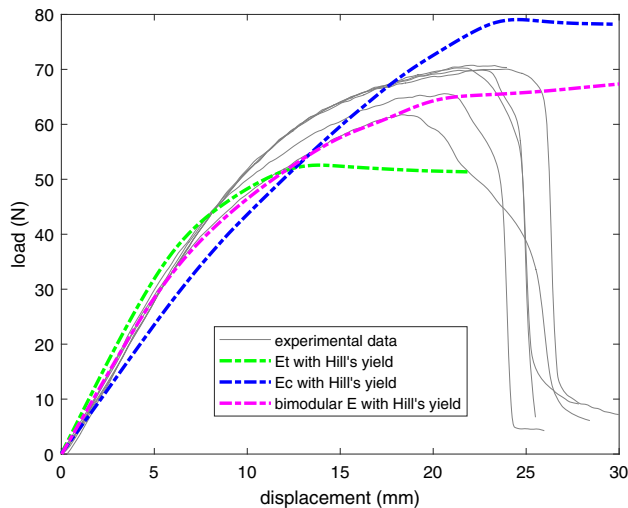
483

Fig. 7. Load vs displacement obtained from the bending experiments and the bending finite elements model with three different material-modulus considerations and Hill's yielding.
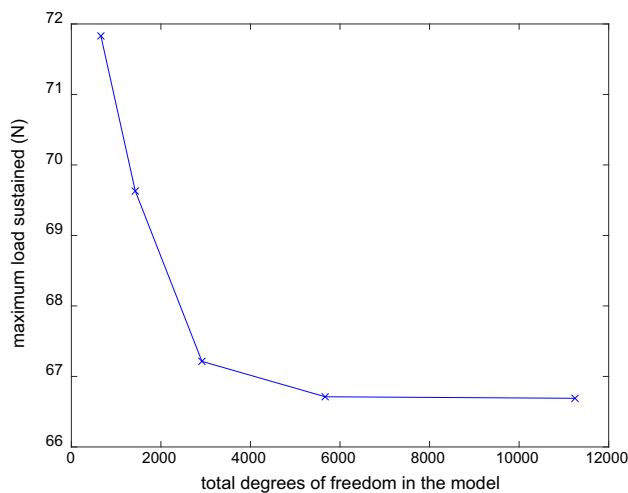

Fig. 8. Mesh convergence for bending test finite element model.

mean displacement at maximum loads obtained from the experimental data.

The model that accounted for the bimodular nature of the material and different yielding behavior in tension and compression predicted maximum load of the beam section at a load of 67.3 N. The model also under-predicted the stiffness in the linear-elastic range by 1.8% compared to the experimental data. Among the three finite element models used, the load–displacement curve obtained from this model was closest to the experimental data.

The early yielding and the lower maximum load are predicted by the model with material properties based on tension tests because the material input properties based on the tension tests have lower

yield stresses compared to those based on the compression tests. Similarly, the higher bending stiffness at lower load is predicted by the model with material properties based on the tension tests because the tensile Young's modulus is higher compared to the compressive Young's modulus. Since the bottom fibers of the beam are in tension and the top fibers are in compression, the results predicted by the model considering the bimodular nature of the material are closest to the experimental results.

The mesh convergence plot for the bending test finite element model with bimodular elasticity and Hill's yielding is shown in Fig. 8.

CONCLUSION

This study extends the existing CLT-based linear-elastic finite element models to 3D printed composites to address the bimodular and elasto-plastic yielding behavior observed in these materials.

The following conclusions have been made:

1. A laminate analysis based finite element modeling method only approximates the linear portion of the stress–strain behavior of the 3D printed composite under tensile loading.
2. An elasto-plastic finite element model with Hill's yield criterion was effective in predicting the overall stress–strain response of the 3D printed composite under tensile loading.
3. A linear elastic finite element analysis based on bimodular behavior was effective in predicting the load–displacement response under three-point bending for the laminate.
4. The bimodular behavior of the material needs to be considered to effectively predict the bending behavior of a 3D printed part.

Future work should involve reducing analysis time. The finite element analysis takes considerable time (about 2 h) to complete. The main reasons for the slow analysis speed are the use of an explicit solver with time steps of about 10^{-6} s, and the unsymmetric stiffness matrix that arises due to the bimodularity of the material. The stress–strain relationships are calculated up to 3 times for each time step for each element. A model using an implicit solver should be considered. The effect of using a symmetric matrix on accuracy can be studied.

REFERENCES

1. X. Wang, M. Jiang, Z. Zhou, J. Gou, and D. Hui, *Compos. B* 110, 442 (2017).
2. ISO/ASTM52900-15, https://doi.org/10.1520/isoastm52900-15.
3. P. Kulkarni and D. Dutta, *J. Eng. Ind.* 121, 93 (1999). https://doi.org/10.1115/1.2830582.
4. J.F. Rodríguez, J.P. Thomas, and J.E. Renaud, *J. Mech. Des* 125, 546 (2003).
5. F. Yang and R. Pitchumani, *Macromolecules* 35, 3213 (2002).
6. G. Alaimo, S. Marconi, L. Costato, and F. Auricchio, *Compos. B* 113, 371 (2017).
7. S. Timoshenko, *Strength of Materials, Part II: Advanced theory and problems*, (Van Nostrand Reinhold, 1958), pp 1-510.
8. C.W. Bert and C.J. Rebello, *Eng. Str.* 5, 227 (1983).
9. R.M. Jones, *AIAA J.* 15, 16 (1977).
10. N. Phan-Thien, *Fibre Sci. Technol.* 14, 191 (1981). https://doi.org/10.1016/0015-0568(81)90011-7.
11. C. Ziemian, M. Sharma and S. Ziemian, in *Mechanical Engineering*, *InTechOpen*, (2012) https://doi.org/10.5772/34233.
12. Y. Song, Y. Li, W. Song, K. Yee, K.Y. Lee, and V.L. Tagarielli, *Mater. Des.* 123, 154 (2017).
13. J.-Y. Sun, H.-Q. Zhu, S.-H. Qin, D.-L. Yang, and X.-T. He, *J. Mat. Sci. Technol.* 24, 1845 (2010). https://doi.org/10.1007/s12206-010-0601-3.
14. C. Bert, *J. Eng. Mater. Technol.* 99, 344 (1977).
15. S. Ambartsumyan and A.A. Khachatryan, *Mekhanika Tverdogo Tela* 2, 44 (1986).
16. M.E. Babeshko and Y.N. Shevchenko, *Intl. Appl. Mech.* 43, 1208 (2007).
17. M. Shi, Y. Zhang, L. Cheng, Z. Jiao, W. Yang, J. Tan, and Y. Ding, *J. Phys. Chem. B.* 120, 10018–10029 (2016).
18. W. Zhang, C. Cotton, J. Sun, D. Heider, B. Gu, B. Sun, and T.-W. Chou, *Compos. B* 137, 51 (2018).
19. M. Somireddy, C.V. Singh, and A. Czekanski, *Exp. Mech.* 59, 871 (2019).
20. M. Destrade, M.D. Gilchrist, J.A. Motherway, and J.G. Murphy, *Mech. Mater.* 42, 469 (2010).
21. S. Bhandari and R. Lopez-Anido, *Prog. Addit. Manuf.* 4, 143 (2018). https://doi.org/10.1007/s40964-018-0070-2.
22. S. Bhandari and R. Lopez-Anido, *Addit. Manuf.* 22, 187 (2018).
23. S. Guessasma, S. Belhabib, H. Nouri, and O. Ben Hassana, *Eur. Polym. J.* 85, 324 (2016).
24. H. Nouri, S. Guessasma, and S. Belhabib, *J. Mater. Process. Technol.* 234, 113 (2016).
25. S. Guessasma, S. Belhabib, and H. Nouri, *Polymers* 11, 125 (2019).
26. N. van de Werken, J. Hurley, P. Khanbolouki, A.N. Sarvestani, A.Y. Tamijani, and M. Tehrani, *Compos. B* 160, 684 (2019).
27. Y. Xu, H. Zhang, B. Šavija, S. Chaves Figueiredo, and E. Schlangen, *Mater. Des.* 162, 143 (2019).
28. M.C. Somireddy Aleksander, *J. Manuf. Mater. Process.* 1, 18 (2017). https://doi.org/10.3390/jmmp1020018.
29. M. Somireddy, A. Czekanski, and C.V. Singh, *Mater. Today Commun.* 15, 143 (2018).
30. K.-S. Liu and S.W. Tsai, *Compos. Sci. Technol.* 58, 1023 (1998).
31. D. Notta-Cuvier, F. Lauro, and B. Bennani, *Int. J. Solids Struct.* 66, 140 (2015).
32. P. Gotsis, C.C. Chamis, and L. Minnetyan, *Compos. Sci. Technol.* 58, 1137 (1998).
33. W.W. El-Tahan, G.H. Staab, S.H. Advani, and J.K. Lee, *J. Eng. Mech.* 115, 963 (1989).
34. L. Chen, W. Wen, and H. Cui, *Sci. China: Technol. Sci.* 56, 89 (2012).
35. L. Zhang, Q. Gao, and H.W. Zhang, *Int. J. Mech. Sci.* 70, 57 (2013).
36. L. Zhang, H.W. Zhang, J. Wu, and B. Yan, *Acta Mech. Sin.* 32, 481 (2015). https://doi.org/10.1007/s10409-015-0517-3.
37. Z. Du, Y. Zhang, W. Zhang, and X. Guo, *Int. J. Solids Struct.* 100, 54 (2016).
38. F. Mollica, M. Ventre, F. Sarracino, L. Ambrosio, and L. Nicolais, *Comput. Math. Appl.* 53, 209 (2007).
39. H. Mehdipour, P.P. Camanho, and G. Belingardi, *Compos. B* 165, 199 (2019).
40. A. Nanda and T. Kuppusamy, *Compos. Struct.* 17, 213 (1991).
41. F. Dunne and N. Petrinic, *Introduction to Computational Plasticity*, (OUP Oxford illustrated, reprint edn., 2005), pp 143-180.
42. F. Hild and S. Roux, *Strain* 42, 69 (2006).
43. C. Niezrecki, P. Avitabile, C. Warren, P. Pingle, M. Helfrick, and E.P. Tomasini, *AIP Conf. Proc.* 1253, 219 (2010). https://doi.org/10.1063/1.3455461.
44. A. Młyniec and T. Uhl, *Proc. Inst. Mech. Eng. Part C* 226, 16 (2011). https://doi.org/10.1177/0954406211411552.